https://doi.org/10.5194/amt-2024-178
Preprint. Discussion started: 28 October 2024

Atmospheric Measurement Techniques Discussions
Open Access
EGU

Characterizing Urban Planetary Boundary Layer Dynamics Using 3-Year Doppler Wind Lidar Measurements in a Western Yangtze River Delta City, China

Tianwen Wei[1], Mengya Wang[1*], Kenan Wu[1], Jinlong Yuan[1], Haiyun Xia[1,2*], Simone Lolli[3]

[1]School of Atmospheric Physics, Nanjing University of Information Science & Technology, Nanjing 210044, China.

[2]School of Earth and Space Science, University of Science and Technology of China, Hefei 230026, China

[3]CNR-IMAA, Contrada S. Loja snc, Tito Scalo (PZ), 85050, Italy

Correspondence to: Mengya Wang (wmengya123@nuist.edu.cn) and Haiyun Xia (hsia@ustc.edu.cn)

Abstract

Understanding the dynamics of the planetary boundary layer (PBL) is crucial for comprehending land-atmosphere interactions. This study utilizes three years of Doppler wind lidar measurements from June 2019 to June 2022 to investigate PBL dynamics over Hefei, a city in the Western Yangtze River Delta, China. We focus on the seasonal and diurnal variations in key characteristics, such as wind profiles, shear intensity, turbulent mixing, low-level jets (LLJs), and mixing layer heights (MLH). Results show that horizontal wind speeds accelerated more rapidly above 3 km, with the predominant westerly winds (270°±15°) in all seasons. The vertical depth of high wind zone (> 8 m s-1) during the day is found generally deeper than at night, particularly in winter. In Hefei, LLJs primarily form at sunset and dissipate by noon, typically at altitudes between 0.5 and 0.6 km throughout the year, except in July. LLJ occurrences are most frequent in spring (31.7%), followed by summer (24.7%), autumn (22.3%), and winter (21.3%). Summer LLJs are most intensified, extending up to 1.5 km. The larger wind gradient below the jets significantly enhances turbulence and shear intensity near the ground at night. The seasonal average MLH peaks between 2:00 p.m. and 3:00 p.m., reaching approximately 1.2 km in spring and summer. Cloud cover raises MLH by about 100 m at night but decreases it by 200 m at the afternoon peak. This study provides insights into lidar-based PBL dynamics and highlights implications for local standards concerning low-altitude economic activities.

1. Introduction

The planetary boundary layer (PBL) refers to the lowest 1~3 km of the atmosphere that is directly influenced by the presence of the underlying surface, and usually responds to surface forcings in an hour or less (Stull, 1988). These surface forcings include frictional drag, heat transfer, pollutant emission, evaporation and transpiration, and terrain induced flow modifications (Garratt, 1994). The depth and structure of the PBL are determined by the physical and thermal properties of the underlying surface as well as the dynamics and thermodynamics of the lower atmosphere (Madala et al., 2014). One of the most important characteristic of the PBL is turbulence, which dominates the vertical exchange of heat, moisture, momentum, trace gases, and aerosols between the free atmosphere and the Earth's surface or regolith (Baklanov et al., 2011; Petrosyan et al., 2011). In the PBL, the sources of turbulent mixing exhibit significant temporal and spatial variations, which include buoyancy (convective mixing), wind shear (mechanical mixing), entrainment at the top of boundary layer, and radiative cooling in stratocumulus clouds (top-down convective mixing) (Ortiz-Amezcua et al., 2022). Such turbulent motion in the PBL has been demonstrated to be inherently connected to air pollution by modulating the dispersion, transport, and accumulation process, and have critical impacts on land-atmosphere energy balance, as well as aerosol-cloud-precipitation interactions (Kim and Entekhabi, 1998; Wang et al., 2001; Chen et al., 2011; Wood et al., 2015; Li et al., 2017; Su et al., 2020, 2018; Christensen et al., 2024).

Hefei, the capital of Anhui province, has experienced incredible economic growth and urban sprawl over the past two decades (Zhao and Zou, 2018). Situated between the Yangtze River and Huaihe River, in what is known as the Jianghuai region, the Hefei Metropolitan Circle plays a pivotal role in the Yangtze River-Huaihe River Water Transfer Project to provide benefits for water supply, transportation, agriculture, and power generation (Li et al., 2019; Zhang et al., 2023). Apart from tremendous economic benefits achieved in Hefei, intense human activities create a profound influence on the local climate, affecting the thermal, hydrological, and wind environments in the PBL within and beyond city limits (Shi et al., 2008; Li et al., 2022a). In this context, the PBL study is vital for better understanding the exchange process between the atmosphere and land over complex underlying surfaces, and improving the parameterization schemes in numerical weather prediction models. However, previous studies mainly focused on surface air pollution characteristics and its associations with meteorological parameters, as well as the impacts on human health based on in-situ monitoring measurements or air quality modelling (Hu et al., 2024; Qin et al., 2017; Shen et al., 2022; Zhang et al., 2017; Zhu et al., 2019). Among various observation techniques, the lidar is a powerful tool and has been applied in retrieve vertical profiles of PBL properties in Hefei, such as aerosols, winds, turbulence, precipitation, temperature, and water vapor during a period (Zhou, 2002; Xia et al., 2015, 2016; Wei et al., 2021, 2022; Jiang et al., 2022; Yuan et al., 2020; Wang et al., 2015b). Therefore, it is essential to utilize the long-term lidar measurement to characterize the PBL dynamics such as winds and turbulence sources to further understand the land-atmosphere interaction.

The key parameter of PBL meteorology is the PBL height (PBLH) which displays significant spatiotemporal variability under different atmospheric and surface conditions (Guo et al., 2019; Zhang et al., 2022; Zhao et al., 2023). It strongly depends on surface characteristics such as surface heating rate, strength of winds, topography, surface roughness, free atmospheric characteristics, the amount of clouds and moisture (Kotthaus et al., 2023; Zhang et al., 2020). Multiple approaches have been developed to determine the PBLH based on observations, such as in situ radiosonde (Gu et al., 2022; Guo et al., 2021; Yue et al., 2021), aerosol-based and dynamic-based lidar techniques (Chen et al., 2022; Huang et al., 2017; Vivone et al., 2021; Wang et al., 2020, 2021; Yang et al., 2020; Yin et al., 2019). In the practical measurements of PBLH, it is necessary to consider its distinct diurnal cycle of PBL. The PBL can be categorized into three dominant regimes: convective boundary layer (CBL), stable boundary layer (SBL), and residual layer (RL) based on the thermodynamic stability in the lower atmosphere (Caughey and Palmer, 1979). After sunrise, increasing radiative heating triggers the development of near-surface turbulent eddies and leads to the formation of CBL, which the CBL grows with time and reaches its maxima in the early afternoon. The CBL consists of a convective surface layer, mixing layer (ML) above, and entrainment zone (EZ) at the top (Wyngaard, 1988). After sunset, the radiative cooling creates the SBL close to the surface and its depth grows as night progresses. The RL lies above the SBL meanwhile

https://doi.org/10.5194/amt-2024-178
Preprint. Discussion started: 28 October 2024

Atmospheric Measurement Techniques Discussions

a capping inversion overlies the RL (Fochesatto et al., 2001). However, studies in diurnal and seasonal characteristics of the PBLH under different stable conditions in Hefei based on long-term measurements have not been documented yet, to the best of our knowledge at the writing of this work.

Turbulence in the PBL is generated mechanically by wind shear, and convectively by buoyancy. Wind shear is the main source of turbulence in the nocturnal boundary layer (NBL, also known as the SBL), which can be enhanced in the presence of low-level jets (LLJs). Yang et al. (2023) found that wind shears induced by LLJs often enhanced the vertical mixing processes, reduced the atmospheric stability, and resulted in small weak direction shifts in eastern Idaho, USA. The formation of LLJ can provide a driving force for the development of a deeper CBL on the Tibet Plateau (Su et al., 2024). Many studies investigated the prominent role of LLJs in heavy rainfall events in the Jianghuai region (Chen et al., 2020; Yan et al., 2021; Liu et al., 2022; Cui et al., 2023), but there has been a lack of research specifically focusing on Hefei. The Huaihe River region, including Hefei, is one of the six high-frequency regions of LLJs in China (Yan et al., 2021). The LLJs over China are usually classified into two types: boundary layer jets (BLJs, below 1 km) and synoptic-system-related LLJs (SLLJs, within 1–4 km) (Du et al., 2014). The occurrence of BLJs is associated with significant vertical shear of horizontal wind and diurnal variation. On the contrary, SLLJs are usually related to synoptic-scale weather systems. This study addresses a previous research gap by investigating the characteristics of LLJs formation and types, and vertical wind shear (VWSH) in Hefei, with a focus on their monthly variations across different times and altitudes.

In this paper, we utilize a 3-year Doppler wind lidar measurements to characterize the PBL dynamics in Hefei. The horizontal wind speeds and direction, LLJs, VWSH, turbulent kinetic energy dissipation rate (TKEDR), mixing layer height (MLH) and PBLH are thoroughly analyzed. Remote sensing retrieval of the above PBL parameters have been fully illustrated and validated in our previous studies (Wang et al., 2019, 2021; Wei et al., 2019, 2022; Wang et al., 2024). This paper aims to shed new light on the diurnal and seasonal characteristics of PBL meteorology and turbulence influenced by diurnal cycles, general circulation, the Asian monsoon, and the synoptic systems.

2. Materials and methodology

2.1 Study area and instruments

Hefei, a rapidly developing new first-tier city, is located in Eastern China within central Anhui Province in Figure 1(a). It covers an area of 11465 km^2, comprising four urban districts, one county-level Chaohu city, and four counties. Its topography includes flat plains, gently rolling hills, and major water bodies such as Chaohu Lake to the southeast in Figure 1(b). The city altitude mainly ranges from 15 to 81 m, with the highest point reaching 595 m (Sun and Ongsomwang, 2021). The Dabie Mountain in the southwest introduces varied elevations and complex topographical features that influence regional atmospheric dynamics in Hefei. Anhui province including Hefei, is located across both the eastern monsoon region and the north-south climate transition zone of China. Hence, Hefei is characterized by the typical subtropical monsoon climate with four distinct seasons. The city receives an annual precipitation of ~1000 mm and average temperature of 15.7 °C, with prevailing southeast winds in spring and summer and northwest winds in autumn and winter (Li et al., 2024).

https://doi.org/10.5194/amt-2024-178
Preprint. Discussion started: 28 October 2024

Atmospheric Measurement Techniques Discussions

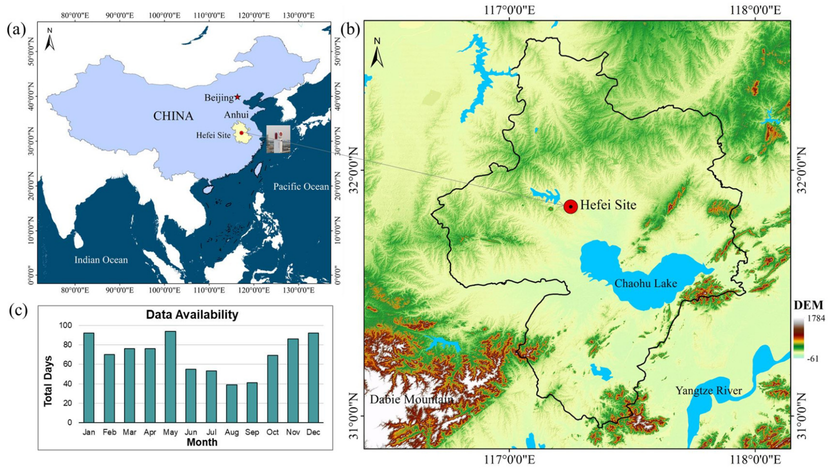

Figure 1. Study area and location of the Doppler wind lidar system. (a) Location (31.83°N, 117.25°E) of Hefei site and administrative boundary of Anhui province; (b) DEM, and the solid black line represents the administrative boundary of Hefei city; (c) Data availability of 3-year Doppler wind lidar measurements. Total days with valid lidar measurements are accounted for each month.

A compact coherent Doppler wind lidar (CDWL) system was deployed on the roof of the School of Earth and Space Science (SESS) building of the University of Science and Technology of China (31.83° N, 117.25°E) in the urban area of Hefei, to monitor the vertical profiles of aerosol, cloud and wind field. The specific location of lidar is referred as Hefei site in Figure 1(a) and Figure 1(b). The lidar system operates at 1.5 μm eye-safe wavelength and uses 300 μJ pulse energy and 10 kHz repetition rate to achieve a maximum detection range of up to 15 km. During the long-term experiment, the lidar performed continuous velocity azimuth display (VAD) scanning mode for high spatial-temporal resolution wind profile measurement. The azimuth angle ranges from 0° to 300° with an interval of 5° and the elevation angle is 60°. The key parameters of the Doppler lidar system are summarized in Table A1 in Appendix. Detailed information about the validation and application of the lidar system can be found in our previous works (Jia et al., 2019; Wei et al., 2020, 2021). The data availability is presented in Figure 1(c) with monthly statistics of total valid days. Note that the lower data availability during the summer seasons is primarily due to frequent rainfall and high temperatures, which caused instability in the lidar systems. However, these issues have been significantly improved in the recently updated systems (Xia et al., 2024).

2.2 Datasets and methods

The CDWL system operated for three consecutive years from June, 2019 to June, 2022, except for some maintenance interruptions (Wang et al., 2024). The number of days available for different seasons and weather types is presented in Table 1, respectively.

Table 1. The days of different weather types during the period of Doppler lidar operation

Weather Types*	Spring	Summer	Autumn	Winter	Total days
Rainy	62	44	37	75	218
Clear	69	21	47	76	213
Cloudy	68	82	50	64	264

Atmospheric Measurement Techniques Discussions

Partly Cloudy	39	38	44	39	160

*__Rainy:__ rain persists for more than 2 hours **Clear:** clouds are present for less than 2 hours.
Cloudy: cloud coverage exceeds 8 hours. **Partly Cloudy:** cloud coverage lasts between 2 to 8 hours.

The time resolution and range gate resolution of the original radial measurements are 1 s and 30 m, respectively. Horizontal wind speed (HWS), horizontal wind direction (HWD), and vertical wind speed (VWS) are retrieved from the measured radial speeds at different azimuth angles using a filtered sin-wave fitting method, based on the assumption of horizontally homogenous wind field (Smalikho, 2003; Banakh et al., 2010; Wei et al., 2020). Considering the duration of one VAD scan, the time resolution of wind profile becomes about 2 minutes. Here, the wind direction of 0° represents the horizontal wind coming from the north, and the angle increases clockwise. The negative (positive) vertical wind speed was defined as upward (downward) motion in this study.

Turbulence activity can be expressed by vertical velocity variance, spectrum width, turbulent kinetic energy, and TKEDR (O'Connor et al., 2010). In this study, we estimate TKEDR using the turbulence statistical model based on the relation between the structure-function of the measured radial velocity and theoretical value (Banakh et al., 2017). The MLH is a significant parameter for presenting the vertical turbulent exchange within the PBL. On the basis of the characteristics of decreasing convective turbulence intensity along with height, the threshold method can effectively determine a typical turbulence height. Here, the MLH is defined as the height up to which TKEDR > 10^{-4} m^2 s^{-3} is reached (Banakh et al., 2021; Wang et al., 2021). In addition, the aerosol-based PBLH, shown in Section 3.6, is also calculated for comparison. It is determined from the aerosol backscatter coefficient using a Harr wavelet method (Caicedo et al., 2017; Kotthaus et al., 2023).

LLJ is a fast air stream with a wind speed maximum in the lowest kilometers of the troposphere (Stull, 1988). Referring the previous studies (Qiu et al., 2023; Zhang et al., 2018; Tuononen et al., 2017) and considering the local characteristics, we identify the LLJs at Hefei using the following criteria: (1) the maximum wind speed $U_{max} >$ 8 m $s^{-1}$and, (2) the wind speed difference $\Delta U = U_{max} - U_{min} >$ 2.6 m s^{-1}, where U_{min} is the minimum wind speed above the height of U_{max}. The LLJ height is then defined as the height of U_{max}. In addition, when a two-layer LLJ exists, the lower one will be selected. Each wind profile was applied to identify the LLJ event. In the statistics procedure of Section 3.3, a time window of 1 h is used to filter out the outliers, and those with fewer than 60% within the window were abandoned.

Vertical wind shear (VWSH) is defined as the change in wind speed and/or direction with height. It can be calculated from the vertical wind profiles using the following equation (Manninen et al., 2018)

$$\mathrm{VWSH} = \frac{(\Delta u^2 + \Delta v^2)^{0.5}}{\Delta z}$$

where the difference in vectors of the wind components u and v is divided by the height difference Δz between the two altitude levels used to compute the wind shear.

https://doi.org/10.5194/amt-2024-178
Preprint. Discussion started: 28 October 2024

Atmospheric Measurement Techniques
Discussions

3. Results

3.1 The 3-year seasonal profiles of the wind frequency

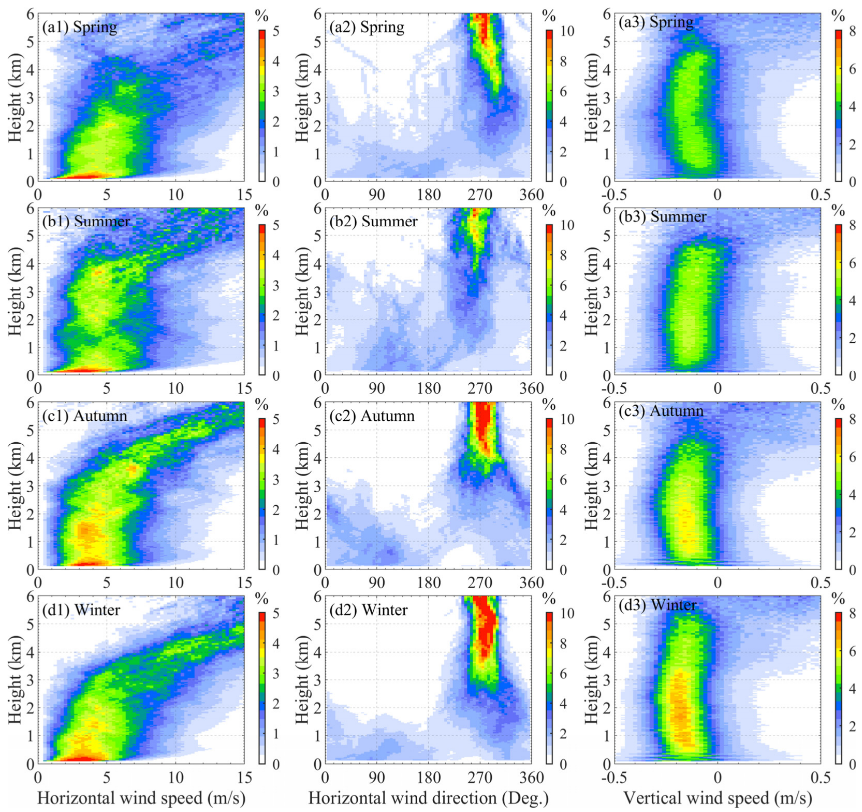

Figure 2. The seasonal frequency distributions of horizontal wind speed (left panel), horizontal wind direction (middle panel), and vertical wind speed (right panel) at different heights below 6 km during (a) Spring: Mar-May; (b) Summer: Jun-Aug; (c) Autumn: Sep-Nov; and (d) Winter: Dec-Feb, at Hefei. Note that the sum of all frequency values along the x-axis equals 100% at any specific height. It should be noted that negative value of vertical wind speed is defined as the upward movement of air.

Vertical wind profiles are influenced by surface friction, terrain, local pressure systems, and global atmospheric circulation patterns. We retrieve the vertical profiles of HWS, HWD, and VWS and calculate the frequency (%) of their occurrence at different heights above ground level (AGL), as shown in Figure 2. The frequency distribution is calculated by the ratio of the counts of wind speeds falling into each bin on the x-axis to the total valid numbers at each height. Therefore, the sum of all frequency values along the x-axis is 100% at any specific height. To represent rich details, the bin size or resolution (i.e., the width of each column) is set to 0.25 m s^{-1}, 5°, and 0.02 m $s^{-1}$for HWS, HWD, and VWS, respectively.

In the left panel of Figure 2, the frequency distribution of HWS (hereafter referred to as HWS%) exhibits a rightward skew in all seasons, a characteristic often modeled using a Weibull or Lognormal distribution due to the non-negative nature of wind speed (Justus et al., 1978; Pobočíková et al., 2017).

https://doi.org/10.5194/amt-2024-178
Preprint. Discussion started: 28 October 2024

Close to the ground, the majority of HWS values are clustered at the lower end, mainly as a result of surface friction. Below ~300 m AGL, HWS increase rapidly as surface friction decreases. From 300 m to 3 km AGL, HWS increases steadily while becoming more dispersed, with the overall distribution (HWS%) spanning between 2 and 7 m s^{-1}. Above 3 km, HWS accelerates more rapidly, particularly in autumn and winter, where HWS% remains relatively concentrated. In contrast, HWS% in spring and summer is more dispersed with a lower frequency of high HWS occurrences (> 10 m s^{-1}). Many studies have demonstrated a significant decrease trend of near surface wind speed in eastern China including Anhui province, induced by large-scale circulation and local land use and land cover change (Li et al., 2018; Liu et al., 2023; Li et al., 2022). Wang et al. (2015) observed that the value of annual mean surface wind speed in Hefei city during 1981-2012 was between 2.0 m s^{-1} and 2.6 m s^{-1} and the highest frequency of maximum surface wind speed occurred in spring. A recent study by Li et al. 2022a analyzed the maximum daily wind speed of 10 minutes from 51 meteorological stations in Anhui province from 2006 to 2020, which showed that the average maximum wind speed in the city of Hefei was between 9.1~17.6 m s^{-1}. Therefore, our results of seasonal HWS values near the ground correspond to previous studies.

The frequency distribution of HWD (hereafter referred to as HWD%) exhibits distinct vertical characteristics, as shown in the middle panel of Figure 2. At higher altitudes (> 3 km), the distribution of HWD is much more concentrated, with predominant westerly winds (270°±15°) in all seasons. Because Hefei city is located between 31°4′ N and 32°38′ N, which is affected by westerly circulation. The finding of prevailing westerlies throughout the year in Hefei is consistent with (Sun et al., 2021). In contrast, the influence of westerlies on HWD% below the PBL is insignificant due to the impact of the underlying surface roughness, terrain distribution, and air flow turbulence. Below 3 km AGL, we can discover notable southwest winds in summer compared to the other seasons. In the summer monsoon season, eastern China (including Hefei city) is mainly dominated by southwest winds, as has been reported by many studies (Liu et al., 2015; Yan et al., 2022; Zhao et al., 2007). Wind directions in the PBL tend to be more variable and chaotic compared to those at higher altitudes. And westerly winds above 1.5 km consistently strengthen with increasing altitude in all seasons.

The right panel of Figure 2 illustrates seasonal profiles of VWS frequency (hereafter referred to as VWS%). The frequency distribution of VWS% is right-skewed and its center lay in negative values between -0.2 m s^{-1} and -0.1 m s^{-1}. The results show that most VWS values are negative below 5 km in all seasons, representing upward motion in the atmosphere. It demonstrates the asymmetric nature of vertical velocities in the atmosphere, where upward movements are stronger than downward movements (Tamarin-Brodsky and Hadas, 2019). Furthermore, Figure 2 (d3) shows that winter has the highest frequency of negative VWS, with most VWS% ranging from 4% to 7% below 3 km AGL. A climatology study of cold frequency suggests that cold fronts are most frequently occurred in cold seasons over Hefei city (Xue et al., 2022). In winter, cold fronts associated with the winter monsoon can enhance upward motion of the air as the heavier (more dense) cool air pushes under the lighter (less dense) warm air (Kang et al., 2019; Parsons, 1992). The upward motion intensifies and is vigorous along the frontal boundaries, leading to cloud formation and precipitation. The higher positive values in the asymmetric distribution of VWS, particularly above 3 km, are attributed to the contribution of falling precipitation particles (Wei et al., 2019). Under these conditions, the detected vertical speed reflects the movement of larger hydrometeors rather than the air motion itself.

https://doi.org/10.5194/amt-2024-178
Preprint. Discussion started: 28 October 2024

3.2 Diurnal HWS profiles in different seasons

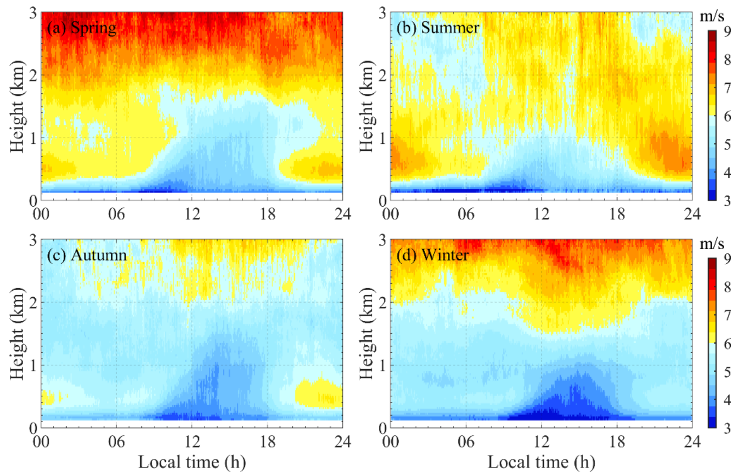

Figure 3. Diurnal profiles of seasonal averaged horizontal wind speeds at different heights below 3 km during (a) Spring: Mar-May; (b) Summer: Jun-Aug; (c) Autumn: Sep-Nov; and (d) Winter: Dec-Feb, at Hefei.

The diurnal variation of the vertical wind profile within the PBL is intricately linked to the dynamics and thermodynamics driven by the daily cycle of solar heating and longwave cooling. Figure 3 illustrates how HWS profile varies with local time (LT) on a seasonal scale. The minimum values of HWS are found in the lowest layer, primarily due to the impact of rough surface.

During the day, solar heating induces turbulence and convection, which increase surface friction and slow down the up-level horizontal wind. This results in the formation of a gentle wind zone (GWZ), characterized by wind speeds below 5 m s^{-1}, a feature that can be observed in all seasons. And the diurnal variation of the GWZ strongly correlates with the development of the mixing layer. At night, radiative cooling generates a temperature inversion, inhibiting vertical mixing and fostering laminar flow with increased shear intensity. Consequently, nocturnal winds are generally stronger than daytime winds at the same height below 1.5 km AGL throughout all seasons. Above this height, the HWS profile is usually more uniform and stronger due to the reduced frictional drag in the free atmosphere. It is interesting to find that the vertical height of high wind zone (> 8 m s^{-1}) during the day is much lower than at night, particularly in winter. In Figure 3d, an appreciable enhancement of HWS at 1.5 km is discovered during the day particularly between 11:00 a.m. and 16:00 p.m., when the PBL tends to grow and become deeper due to radiative heating of the surface. In general, the HWS increases with height. However, as seen in Figures 3(a) to 3(c), a distinct local maximum in HWS, occurring between approximately 0.4 km and 0.8 km, is observed after 8:00 p.m. and before 7:00 a.m. the next day. This is especially pronounced in summer, where the highest values and the highest vertical extent of the wind are recorded. These winds are typically associated with the nocturnal LLJs, a narrow band of strong winds that forms in the lower PBL. Although the seasonal average HWS reflects the overall wind conditions, the pronounced notch structure in the profile underscores the frequent occurrence of LLJs, which will be explored in more detail in the next section.

3.3 Monthly characteristics of LLJ at different times and heights

LLJ is characterized by a concentrated band of strong winds located in the lower part of the

https://doi.org/10.5194/amt-2024-178
Preprint. Discussion started: 28 October 2024

atmosphere. The diurnal variation of its formation and occurrence is influenced by the interaction between surface heating/cooling cycles, atmospheric stability, and synoptic-scale weather patterns. Figure 4(a) illustrates the statistical frequency (%) of the occurrences of LLJs at different hours for each month. Frequency values are calculated as the ratio of the total number of LLJ occurrences to the total number of available days in the specific month over a 3-year period. Additionally, the monthly variation of the sunrise, noon, and sunset time was also plotted. Figure 4(b) presents the frequency distribution (%) of LLJs occurrences over the height for each month, with the sum of each column equaling 100%. The wind rose charts of the LLJ events for the four seasons are presented in Figure 5(a)~(d), respectively. The seasonal and intraseasonal variability of predominant wind directions and wind speeds of LLJs are influenced by general circulation, the East Asian monsoon, and synoptic systems. The spatial distributions of the 500-hPa geopotential height and geopotential height anomalies are presented in Figure A1.

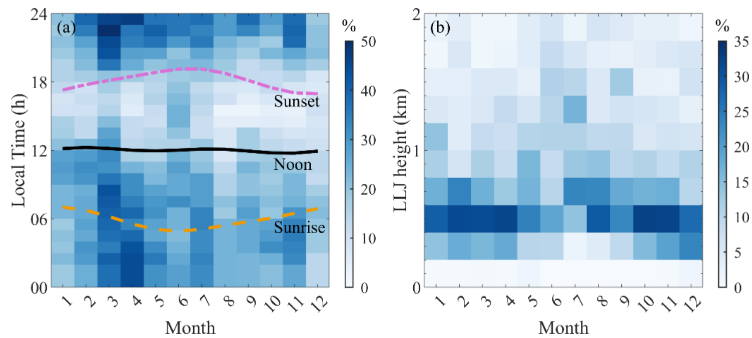

Figure 4. (a) The frequency (%) of LLJs occurrences at different times for each month. The purple dot-dashed line, the black solid line, and the orange long-dashed line refer to the mean sunset, noon, and sunrise times for each month, respectively. (b) The frequency distribution of LLJ occurrence over the height for each month, with the sum of each column equal to 100%.

Generally, LLJs occurrences are most frequent in spring, followed by summer, autumn, and winter in Hefei. The average seasonal LLJs frequencies were 31.7%, 24.7%, 22.3%, and 21.3% in spring, summer, autumn, and winter, respectively. In Figure 4(a), the sunrise and sunset times exhibit monthly variation due to the Earth's revolution around the Sun. We refer to the period between sunset and sunrise as daytime, and the period between sunset and the next sunrise as nighttime. LLJs are more frequently observed during the night and early morning throughout all months. In the classical theoretical description of inertial oscillations, LLJs develop because of the decoupling of nocturnal winds from the surface friction, facilitated by the formation of a near-surface temperature inversion (Blackadar, 1957). At night, the surface cools more rapidly than the air above, giving a rise to the formation of temperature inversions. It causes the air above the temperature inversion to decouple from the surface's frictional effects (Mirza et al., 2024). The weaker friction enables an acceleration of wind aloft with the development of a pronounced super-geostrophic wind speed maximum. Such undisturbed inertial oscillations are a widely known formation mechanism of nocturnal LLJ (NLLJ) (Sisterson and Frenzen, 1978). LLJs are often most pronounced during the early morning hours, typically before the onset of daytime heating. During this time, the temperature inversion is typically strongest because nocturnal cooling has been ongoing for several hours. After sunrise, the onset of daytime heating gradually disrupts the stable boundary layer, reducing the occurrences of LLJ formation. Consequently, LLJs are less

https://doi.org/10.5194/amt-2024-178
Preprint. Discussion started: 28 October 2024

frequent between noon and sunset.

In Figure 4(b), more than 70% of LLJs commonly occur at heights ranging from 0.3 km to 0.8 km AGL in all seasons except summer. The vertical distribution of LLJs occurrences frequency in this study also corresponds to previous studies. For example, Yan et al. (2021) found that 400 m AGL was the most frequent height for the jet-nose appearing in the Huaihe River Basin. Wei et al. (2013) revealed that 76% of the observed LLJs were found to occur at an average altitude below 600 m in the Yangtze River Delta region. Following the classification of (Rife et al., 2010), the dominant type of LLJs in Hefei can be identified as BLJs that occur mainly in the PBL below 1 km AGL. The highest occurrence frequency of LLJs appeared between 0.5 km and 0.6 km AGL in all months other than July, with peak heights between 0.7 and 0.8 km AGL. The frequency of LLJs occurrences varies with months and heights in Hefei. LLJs occurrences are most frequent during spring months, with decreasing frequency from March to May. Our results are consistent with Yan et al. (2021), who found that LLJs were the most frequent in spring in Huaihe River Basin based on long-term radiosonde observations from 2011 to 2017. The driving mechanisms to LLJs include inertial oscillations under stable stratification, fronts and baroclinic weather patterns in flat terrain, orographic and thermal effects in complex terrain. Considering the topography and weather patterns, Hefei is prone to cyclones throughout the year, so the Asian monsoon system and synoptic processes may be the most important influential factors in LLJs activities. In contrast, previous studies on the LLJ climatology over other typical regions or cities showed different seasonal variations of LLJs occurrences. For example, LLJs occur more often in spring and winter in Beijing while those appear more frequently from October to December and from February to April in Guangzhou using long-term wind profiler observations (Miao et al., 2018).

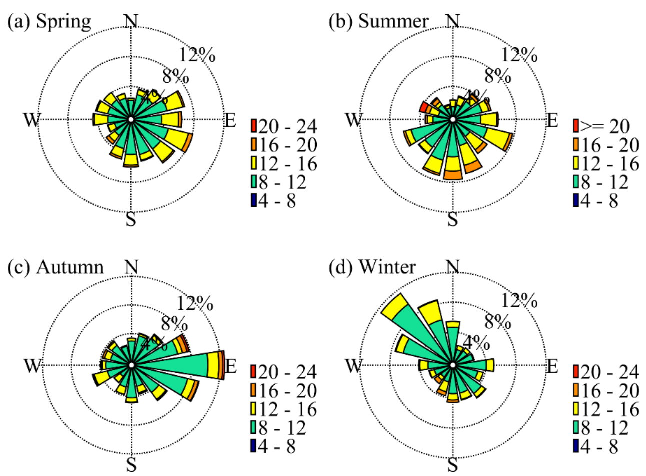

Figure 5. Wind rose charts for total LLJ events accounted for each season at Hefei. (a) Spring: Mar-May; (b) Summer: Jun-Aug; (c) Autumn: Sep-Nov; and (d) Winter: Dec-Feb.

Figure 5(a) shows that the dominant wind directions of LLJs during spring are from the east (E) to the southeast (SE). Furthermore, the maximum HWS of LLJs reaches up to 20 m s^{-1} with more than half of HWS exceeding 12 m s^{-1}. The varying dominant wind directions are associated with the transition from the influence of the East Asian winter monsoon (EAWM) to its summer phase over Hefei. LLJs occurrences peak in March due to its unique atmospheric conditions. During this time, the influence of the winter monsoon is waning, but the full onset of the summer monsoon has not yet occurred. This

https://doi.org/10.5194/amt-2024-178
Preprint. Discussion started: 28 October 2024

Atmospheric Measurement Techniques Discussions

environment of a mix of cold and warm air masses is particularly favorable for LLJs formation. Compared to March, LLJs occurrences are less frequent in April and May as the East Asian Summer Monsoon (EASM) begins to take hold. As spring progresses, the strong baroclinic conditions that favors LLJs formation begin to weaken. Because the temperature gradient between the cold north and the warming south decreases driven by the growing influence of the western Pacific Subtropical High (WPSH).

The overall occurrence frequency of LLJs during summer is lower than that in spring, but their intensity is the strongest. In Figure 5(b), the predominant wind directions of LLJs are from the south (S) and the east-southeast (ESE) with peak HWS reaching 20 m s^{-1}. During summer, the fully established EASM is favorable for LLJs formation. Furthermore, the WPSH system extends northwestward from the western Pacific Ocean towards eastern China, stabilizing the atmospheric conditions that favors LLJs formation. The stronger the WPSH, the more intense the pressure gradient, which can lead to stronger southeast-west winds at low levels. The LLJs occurrence generally peak in July, followed by June and August. In July, the EASM is typically at the peak and the WPSH is usually at its most expansive and positioned to exert the strongest influence over eastern China, including Hefei.

LLJs occurrences are less frequent during autumn and winter compared to spring and summer. Figure 5(c) shows the predominant easterly wind direction (>12%) of LLJs throughout all autumn months, with the maximum HWS reaching up to 24 m s^{-1}. As autumn approaches, the EASM transitions to the EAWN and the WPSH further shifts eastward and southward (Figure A1). This shift exerts a weaker but persistent influence that channels the air from the east. The least frequency of LLJs occurrences in winter could be associated with general calm wind conditions in the lower troposphere (Figure 3d) and large-scale synoptic systems, like cold fronts and high-pressure systems. These systems may not be conducive to the formation of LLJs which typically require a specific set of atmospheric conditions, such as stable conditions and wind shear. During winter, the predominant wind direction of LLJs during winter was from the northwest (NE) in Figure 5(d), which is due to the dominance of the EAWN. The prevailing NE wind of LLJs in winter was not as strong as in the other seasons, with maximum HWS reaching 16 m s^{-1}. Therefore, LLJs in Hefei are dominated by southwesterly winds in summer and northeasterly winds in winter.

3.4 Diurnal cycle of VWSH profiles for each season

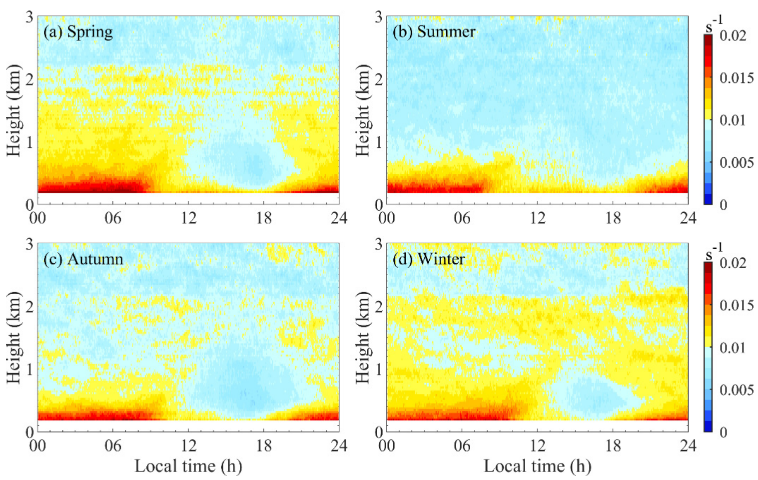

Atmospheric Measurement Techniques Discussions

Figure 6. The same as in Fig. 3 but for VWSH.

VWSH depends directly on vertical wind profiles and exhibits both diurnal and seasonal variations within the boundary layer, as shown in Figure 6(a)~(d). Due to surface friction, the wind speeds decrease within the urban canopy, eventually reaching zero at ground level. These rapid changes in wind speed create a large wind speed gradient, resulting in an increased shear intensity in the surface layer. Throughout all seasons in Hefei, high VWSH values exceeding 0.015 m s^{-1} per meter (hereafter denoted by s^{-1}) are typically observed below 0.4 km.

Below 0.5 km, VWSH decreases from sunrise to the afternoon due to surface heating and increased atmospheric mixing, which consequently led to a more uniform wind profile (Figure 3). In contrast, it increases from sunset to early morning as surface cooling induces a temperature inversion, which creates a stable boundary layer where winds aloft decouple from the surface. At night, a sharper wind speed gradient with height is created under fully developed stable boundary layer, leading to maximum VWSH in this layer. In the low to mid-level atmosphere (0.5~1 km), VWSH also varies diurnally, with relatively lower values compared to VWSH below 0.5 km. Daytime VWSH in this layer is generally due to the well-mixed boundary layer. But it can vary depending on local weather conditions and synoptic influences. At night, high VWSH values above 0.01 s^{-1} is usually associated with the presence of a LLJ and/or a strong temperature inversion, with the maximum VWSH typically occurring just below the core of the LLJ. In the upper level (> 1 km), VWSH is less influenced by the diurnal cycle and remained relatively stable throughout the day. However, high VWSH can still occur in this layer when it is coupled with LLJs or influenced by large-scale synoptic systems.

The seasonal variation of VWSH is closely linked to the region's climatic patterns, particularly the influence of the East Asian monsoons, which drive significant changes in temperature, wind patterns, and atmospheric stability throughout the year. In general, high VWSH values (> 0.015 s^{-1}) near the surface are related to LLJs occurrences across all seasons. On the contrary, VWSH values above 1 km in spring and winter are significantly larger compared to summer and autumn, which spatial pattern also corresponds to vertical distributions of seasonal HWS profiles. During the two seasons, Hefei often receives invasion of cold air/surge events, leading to strong winds. In winter, Hefei experiences strong VWSH primarily due to the impact of the EAWM and large-scale synoptic systems, such as cold fronts and jet-streams. Weaker solar heating in winter results in less pronounced diurnal variation of VWSH. These synoptic systems also lead to significant VWSH (> 0.01 s^{-1}) above 1 km, which is characterized by strong winds aloft. In spring, Hefei experiences strong VWSH due to the transitional atmospheric conditions of the season. The diurnal variation shows a decrease in VWSH after 8:00 a.m. in the morning compared to winter (Figure 6a). The variability in wind directions and speeds contributed to fluctuating VWSH above 1 km influenced by shifting synoptic-scale systems and developing convective activity in late spring.

In contrast, relatively lower VWSH values between 0.005 s^{-1} and 0.01 s^{-1} above 1 km are observed in summer. The weather is dominated by the summer monsoon flow and localized convective systems. These conditions result in a generally weaker VWSH with less pronounced diurnal variation compared to other seasons. Due to significant vertical convective mixing, the wind profile becomes more uniform, resulting in weaker VWSH above 1 km (Figure 6b). As the influence of the winter monsoon begins to dominate, the strong winds aloft and weak surface winds contribute to an increasing VWSH in autumn compared to summer (Figure 6c). Similar to winter, VWSH in autumn is more pronounced at night and early morning due to the formation of temperature inversions. During the day, the reduction in VWSH driven by vertical mixing is less noticeable than in summer, as the overall atmospheric stability increases.

https://doi.org/10.5194/amt-2024-178
Preprint. Discussion started: 28 October 2024

Atmospheric Measurement Techniques
Discussions

3.5 Seasonal characteristics of the diurnal TKEDR profiles

As one of the characteristic features of the atmospheric turbulence, the TKEDR plays a crucial role in boundary layer parameterization schemes. It determines the rate at which turbulent kinetic energy is converted into thermal energy, directly influencing the vertical fluxes of momentum, heat, and mass. Long-term measurements of TKEDR will enhance our understanding of boundary layer dynamic processes and lead to more accurate simulations in atmospheric models.

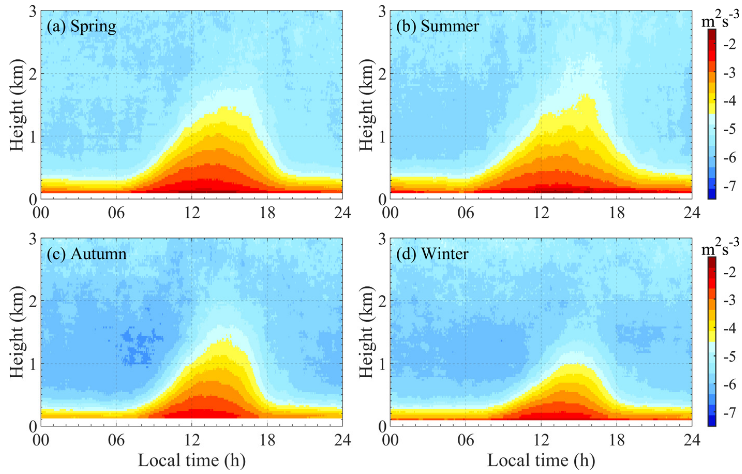

Figure 7. The same as Fig. 3 but for TKEDR.

Figure 7 illustrates the typical diurnal and seasonal cycles of the TKEDR profile. The TKEDR is highest near the surface, with typical values ranging from approximately 10^{-3} to 10^{-2} m^2s^{-3}, depending on the time of day and season. It decreases with height due to the diminishing influence of surface friction and thermal stratification. The convective boundary layer (or mixing layer) is clearly visible by noting where TKEDR is high. Diurnal variation starts from sunrise, as the increased temperature gradient between the surface and the above air enhances thermal buoyancy, which in turn promotes vertical convective mixing and turbulence. This causes TKEDR near the surface to grow and extend toward higher altitudes. In spring and summer, stronger and longer solar radiation leads to a more developed convective boundary layer, both in terms of duration and height, compared to autumn and winter. The convective boundary layer reaches its peak in the early afternoon, then begins to decay after 16:00 p.m., eventually returning to a shallow well-mixed layer near the ground, approximately 350 m in spring and summer, and around 250 m in autumn and winter. During the night, a stable atmospheric layer was formed near the surface and turbulence was primarily driven by mechanical factors (e.g., wind shear) rather than thermal convection. The complex urban surface roughness enhances wind friction, resulting in intensified turbulence, particularly during spring and summer when nocturnal LLJs occur more frequently. This increased turbulence contributes to the elevated TKEDR observed at night during these seasons.

As TKEDR decreases with altitude, its contour lines (though not explicitly plotted but evident from the color gradations in Figure 7) display a right-skewed shape, with a delayed peak time. This delay can be attributed to two factors: first, convective mixing activity takes time to propagate upward from the surface. Second, the ground cools more rapidly than the air in the late afternoon. Consequently, turbulence at higher altitudes lags low-level activity, reflecting the thermal-driven development of

https://doi.org/10.5194/amt-2024-178
Preprint. Discussion started: 28 October 2024

turbulence and energy within the atmospheric boundary layer.

Here, we define the top of the convective boundary layer as the height where TKEDR reaches 10^{-4} m^2s^{-3}. It should be noted that this height can be different from the MLH given in the next section (Sect. 3.6), where the seasonal average MLH is calculated from the daily MLHs. We can see that the top of the convective boundary layer during daytime in summer exhibits dramatic fluctuations, as shown in Figure 7(b), which cloud be attributed to the deep convective activities in the afternoon. Unstable atmospheric stratification enhances vertical convection, leading to the formation of local convective clouds and thunderstorms. These clouds reduce the amount of solar radiation reaching the surface, causing localized cooling. Additionally, this process exacerbates the unevenness in the horizontal distribution of temperature in the affected areas.

Overall, these seasonal and diurnal variations in TKEDR highlight the complex interactions between surface properties, atmospheric stability, and weather systems in shaping the turbulence characteristics within the boundary layer.

3.6 Seasonal variation of diurnal MLH for clear and cloudy days

The diurnal variations of MLH and BLH across different seasons in Hefei are depicted in Figure 8(a) and (b), respectively. The MLH is based on turbulence activities, while the BLH is based on the vertical distribution of material (here aerosol). Therefore, both reflect the diurnal cycle of atmospheric boundary layer dynamics, but there are some differences.

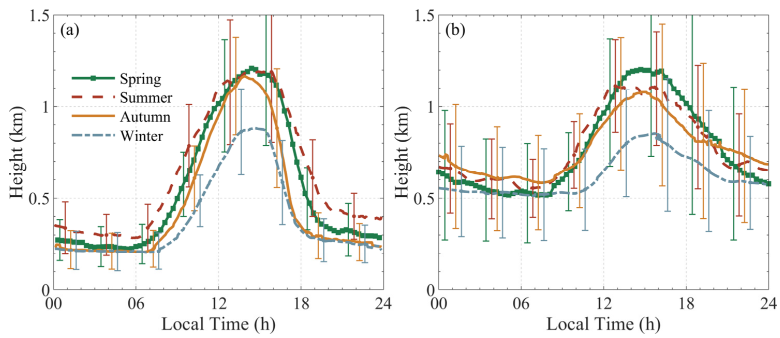

Figure 8. Time series plots of the seasonal average (a) MLH and (b) BLH at Hefei. The error bars represent one standard deviation $\pm\sigma$, and their positions (corresponding to time) vary slightly in different seasons to facilitate comparison.

After sunrise, surface heating induced by solar radiation promotes the devolvement of vertical convective mixing, and drives the surface aerosols upward. When the temperature gradient between the surface and air reaches its maximum, the MLH rises fastest, which appears at about 9:00-10:00 a.m. This time varies with seasons, just as the sunrise time, with the earliest in summer, followed by spring, autumn, and winter. The value of MLH at a certain time also shows the same seasonal relationship, except for the afternoon in summer. Although solar radiation is highest at noon, the short-wave incident radiation received by the surface in the afternoon is still greater than the long-wave outgoing radiation. Therefore, the MLH continues to grow, reaching its maximum between 2:00 p.m. and 3:00 p.m. with about 1.2 km in spring and summer, slightly lower in autumn, and 0.8 km in winter.

The similar afternoon peak of MLH between summer and spring could be attributed to several factors. In the northern hemisphere, the summer solstice which occurs around June 21st or 22nd, is

https://doi.org/10.5194/amt-2024-178
Preprint. Discussion started: 28 October 2024

relatively close to the spring period. This timing means that the transition from spring to summer is not always abrupt. Furthermore, high surface temperatures and increased evapotranspiration during summer lead to frequent convective clouds and precipitation. These factors reduce solar radiation received by the ground and weaken convective mixing, which can suppress the MLH. As a result, the seasonally averaged MLH reflects these cloudy conditions, leading to a peak height that may not be as high as one might expect on clear days.

In the late afternoon, as surface temperatures decrease due to radiative cooling, vertical convection weakens and turbulence kinetic energy dissipates more rapidly, leading to a faster decline in MLH compared to its increase in the morning. Meanwhile, the decrease in BLH is more gradual due to the slower rate of dry deposition of aerosols. It is noteworthy that the BLH curves exhibit larger fluctuations and significantly higher standard deviations compared to the MLH curves. This is primarily due to the considerable retrieval uncertainty in BLH measurements, which are influenced by aerosol distribution. Transboundary aerosols, clouds, and multilayer aerosols (e.g., residual layer) frequently affect these measurements, a well-recognized issue with aerosol-based BLH retrieval methods (Dang et al., 2019; Mei et al., 2022; Kotthaus et al., 2023).

During the night, the temperature inversion layer inhibits vertical thermal convection and mixing. Instead, mechanical mixing driven by wind shear becomes predominant, especially in the presence of low-level jets. Consequently, the MLH is typically highest in summer at about 0.3 km, followed by spring, and lowest in autumn and winter, about 0.2 km. In contrast, The BLH remains higher than the MLH, at approximately 0.5~0.7 km. The higher nocturnal BLH in autumn may be related to the transboundary transport of aerosols and meteorological factors. Both the MLH and the BLH continue to decrease and reach their minimum at sunrise in the next diurnal cycle.

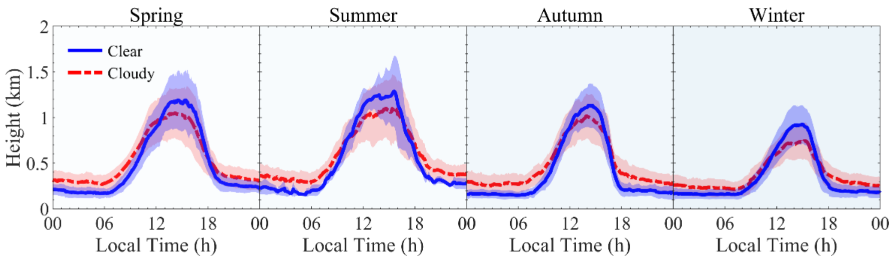

Figure 9. Time series plots of the seasonal average MLH (line) and one-sigma standard deviation (shaded area) for clear days and cloudy days during each season at Hefei, respectively.

To further investigate the influence of clouds on the development of MLH, we compared the seasonally averaged diurnal MLH under different weather conditions, as shown in Figure 9. The diurnal MLH showed significant differences between clear and cloudy days, and exhibited similar characteristics in each season. Overall, the diurnal variation of the MLH was less pronounced on cloudy days with a flatter curve, due to the modulation of clouds on the surface radiation budget. During daytime, the presence of clouds typically reduces surface heating by solar radiation, which inhibits the development of vertical convective mixing and results in a shallower mixed layer compared to clear weather conditions. The difference of MLH reaches its maximum of about 200 m in the afternoon. While during the night, clouds act as a "greenhouse" by absorbing longwave radiation from the ground and slowing down the radiative cooling, which results in a higher MLH compared to clear days. The mean difference in MLH between cloudy and clear days is about 100 m.

Note that, the diurnal MLH in summer showed relatively large variations, particularly on clear days. This variability can be attributed to strong and variable convective activity, as well as to the limited number of data samples. Plum rains and frequent convective clouds in summer lead to a much lower proportion of sunny days than in other seasons.

4. Summary and Conclusions

In this study, three years of Doppler wind lidar measurements (spanning from June 2019 to June 2022) were utilized to characterize the PBL dynamics over Hefei City in western YRD, China. Compared to aerosol lidars, the CDWL is capable of providing additional Doppler information including vertical wind profiles, wind shear intensity, and turbulence mixing, with high spatiotemporal resolution. Moreover, we identified LLJs events based on the nose characteristic of wind speed and retrieved both the turbulence-based MLH and the aerosol-based BLH. Both seasonal and diurnal variations of these key parameters were comprehensively analyzed to shed new insights into the structure and dynamics of the PBL. The results are summarized as follows:

(1) Seasonal characteristics of wind profile: The frequency distribution of HWS exhibited a rightward skew in all seasons, with lower values near the ground, and with a steady increase from 2 to 7 m s^{-1} between 300 m and 3 km AGL, and a more rapid acceleration above 3 km. HWS% profiles in spring and summer were more dispersed, with a lower frequency of high HWS occurrences (HWS > 10 m s^{-1}) above 3 km. Seasonal HWD% profiles showed a predominance of westerly winds (270°±15°) above 3 km, while HWD within the PBL was more variable and chaotic. Seasonal VWS% profiles also exhibited a right-skewed pattern with central values ranging between -0.2 m s^{-1} and -0.1 m s^{-1}, indicating upward motion. Winter, influenced by cold fronts associated with the winter monsoon, had the highest frequency of negative VWS values, ranging from 4% to 7% below 3 km AGL.

(2) Diurnal characteristics of wind profile: A typical GWZ (HWS < 5 m s^{-1}) formed in the PBL during the day in all seasons, with its diurnal variation strongly correlated with the development of the mixing layer. The vertical height of high wind zone (> 8 m s^{-1}) during the day was much lower than at night, particularly in winter, reaching 1.5 km between 11:00 a.m. and 4:00 p.m. In all seasons except winter, a distinct local maximum in HWS between 0.4 km and 0.8 km was observed after 8:00 p.m. and before 7:00 a.m. the next day. The phenomenon was most pronounced in summer due to the influence of nocturnal LLJs.

(3) Monthly characteristics of LLJs: The dominant type was identified as BLJs in Hefei, with occurrences being most frequent in spring (31.7%), followed by summer (24.7%), autumn (22.3%), and winter (21.3%) in. LLJs were more frequently during the night and early morning throughout the year, with 70% typically occurring at heights ranging from 0.3 km to 0.8 km AGL in all seasons except summer. The highest occurrence frequency of LLJs appeared between 0.5 km and 0.6 km AGL in all months other than July, with peak heights between 0.7 and 0.8 km AGL. Predominant wind directions of LLJs were from the E and SE in spring, from S and ESE in summer, from E in autumn, and from NE in winter. LLJs in summer were most intensified with largest frequency of high HWS (>16 m s^{-1}) and extended to altitudes of up to 1.5 km.

(4) Seasonal and diurnal characteristics of VWSH, TKEDR, and BLH: High VWSH values exceeding 0.015 s^{-1} were typically observed below 0.4 km, which was usually associated with the LLJs and/or strong temperature inversions at night. VWSH values above 1 km were significantly larger in spring and winter compared to summer and autumn, correlating with vertical distributions of seasonal HWS profiles. Strong wind speed gradients below and above the LLJs induced large vertical wind shear

intensity (up to 0.02 s^{-1}) and TKEDR (up to 10^{-3} m^2s^{-3}) in the near-surface layer at night. TKEDR was generally highest near the surface, ranging from 10^{-3} to 10^{-2} m^2s^{-3} in all seasons. The BLH exhibited larger fluctuations and greater standard deviations compared to the MLH. The peak MLH occurred between 2:00 p.m. and 3:00 p.m., reaching ~1.2 km in spring and summer, slightly lower in autumn, and around 0.8 km in winter. After sunset, it eventually returned to a shallow well-mixed layer near the ground (~350 m in spring and summer, and ~250 m in autumn and winter). Compared to clear days, cloud cover reduces the MLH by about 200 m at the afternoon peak time, while increasing it by approximately 100 m at night.

In conclusion, these analyses highlight the characteristics of PBL dynamics and their complex interactions with surface heating/cooling, atmospheric stability, and synoptic-scale weather patterns. The long-term statistical results will not only advance scientific understanding, but will also serve as essential references for formulating local standards and regional delineation, including vertical zoning, related to low-altitude economic activities, such as wind energy and drone logistics.

Data Availability. The Doppler wind lidar data used in this study can be provided for non-commercial research purposes upon request to the first author (Tianwen Wei: twwei@nuist.edu.cn) . The ERA5 data sets are publicly available from the ECMWF website at https://cds.climate.copernicus.eu.

Author contributions. Tianwen Wei: Conceptualization, Methodology, Data curation, Formal analysis, Visualization, Writing – review & editing. Mengya Wang: Conceptualization, Writing – original draft, Methodology, Investigation. Kenan Wu: Resources, Data curation. Jinlong Yuan: Resources, Data curation. Haiyun Xia: Conceptualization, Supervision, Resources, Validation. Simone Lolli: Writing – review & editing, Validation.

Conflict of Interest. Some authors are members of the editorial board of Atmospheric Measurement Techniques.

Financial support. This work was supported by the National Natural Science Foundation of China (42405136), the Natural Science Research of Jiangsu Higher Education Institutions of China (23KJB170012).

Reference

Baklanov, A. A., Grisogono, B., Bornstein, R., Mahrt, L., Zilitinkevich, S. S., Taylor, P., Larsen, S. E., Rotach, M. W., and Fernando, H. J. S.: The nature, theory, and modeling of atmospheric planetary boundary layers, Bull. Am. Meteorol. Soc., 92, 123–128, https://doi.org/10.1175/2010BAMS2797.1, 2011.

Banakh, V. A., Brewer, A., Pichugina, E. L., and Smalikho, I. N.: Measurements of wind velocity and direction with coherent doppler lidar in conditions of a weak echo signal, Atmospheric Ocean. Opt., 23, 381–388, https://doi.org/10.1134/S1024856010050076, 2010.

Banakh, V. A., Smalikho, I. N., and Falits, A. V.: Estimation of the turbulence energy dissipation rate in the atmospheric boundary layer from measurements of the radial wind velocity by micropulse coherent doppler lidar, Opt. Express, 25, 22679, https://doi.org/10.1364/oe.25.022679, 2017.

Banakh, V. A., Smalikho, I. N., and Falits, A. V.: Estimation of the height of the turbulent mixing layer from data of doppler lidar measurements using conical scanning by a probe beam, Atmospheric Meas. Tech., 14, 1511–1524, https://doi.org/10.5194/amt-14-1511-2021, 2021.

Blackadar, A. K.: Boundary layer wind maxima and their significance for the growth of nocturnal inversions, Bull. Am. Meteorol. Soc., 38, 283–290, https://doi.org/10.1175/1520-0477-38.5.283, 1957.

Caicedo, V., Rappenglück, B., Lefer, B., Morris, G., Toledo, D., and Delgado, R.: Comparison of aerosol lidar retrieval methods for boundary layer height detection using ceilometer aerosol backscatter data, Atmospheric Meas. Tech., 10, 1609–1622, https://doi.org/10.5194/amt-10-1609-2017, 2017.

Caughey, S. J. and Palmer, S. G.: Some aspects of turbulence structure through the depth of the convective boundary layer, Q. J. R. Meteorol. Soc., 105, 811–827, https://doi.org/10.1002/qj.49710544606, 1979.

Chen, S., Tong, B., Russell, L. M., Wei, J., Guo, J., Mao, F., Liu, D., Huang, Z., Xie, Y., Qi, B., Zhang, H., Sun, Y., Zhang, B., Xu, C., Wu, L., and Liu, D.: Lidar-based daytime boundary layer height variation and impact on the regional satellite-based PM2.5 estimate, Remote Sens. Environ., 281, 113224, https://doi.org/10.1016/j.rse.2022.113224, 2022.

Chen, Y., Zhang, A., Zhang, Y., Cui, C., Wan, R., Wang, B., and Fu, Y.: A heavy precipitation event in the Yangtze River basin led by an eastward moving tibetan plateau cloud system in the summer of 2016, J. Geophys. Res. Atmospheres, 125, e2020JD032429, https://doi.org/10.1029/2020JD032429, 2020.

Chen, Y.-C., Xue, L., Lebo, Z. J., Wang, H., Rasmussen, R. M., and Seinfeld, J. H.: A comprehensive numerical study of aerosol-cloud-precipitation interactions in marine stratocumulus, Atmospheric Chem. Phys., 11, 9749–9769, https://doi.org/10.5194/acp-11-9749-2011, 2011.

Christensen, M. W., Wu, P., Varble, A. C., Xiao, H., and Fast, J. D.: Aerosol-induced closure of marine cloud cells: enhanced effects in the presence of precipitation, Atmospheric Chem. Phys., 24, 6455–6476, https://doi.org/10.5194/acp-24-6455-2024, 2024.

Cui, C., Zhou, W., Yang, H., Wang, X., Deng, Y., Wang, X., Xu, G., and Wang, J.: Analysis of the characteristics of the low-level jets in the middle reaches of the Yangtze River during the mei-yu season, Adv. Atmospheric Sci., 40, 711–724, https://doi.org/10.1007/s00376-022-2107-1, 2023.

Dang, R., Yang, Y., Li, H., Hu, X.-M., Wang, Z., Huang, Z., Zhou, T., and Zhang, T.: Atmosphere boundary layer height (ABLH) determination under multiple-layer conditions using micro-pulse lidar, Remote Sens., 11, 263, https://doi.org/10.3390/rs11030263, 2019.

Du, Y., Zhang, Q., Chen, Y., Zhao, Y., and Wang, X.: Numerical simulations of spatial distributions and diurnal variations of low-level jets in China during early summer, J. Clim., 27, 5747–5767, https://doi.org/10.1175/JCLI-D-13-00571.1, 2014.

Fochesatto, G. J., Drobinski, P., Flamant, C., Guedalia, D., Sarrat, C., Flamant, P. H., and Pelon, J.: Evidence of dynamical coupling between the residual layer and the developing convective boundary layer, Bound.-Layer Meteorol., 99, 451–464, https://doi.org/10.1023/A:1018935129006, 2001.

Garratt, J.: Review: the atmospheric boundary layer, Earth-Sci. Rev., 37, 89–134, https://doi.org/10.1016/0012-8252(94)90026-4, 1994.

Gu, L., Yao, J., Hu, Z., Ma, Y., Sun, F., Yu, H., Wang, S., Yang, Y., Guo, R., and Qin, Y.: Characteristics of the atmospheric boundary layer's structure and heating (cooling) rate in summer over the northern Tibetan Plateau, Atmospheric Res., 269, 106045, https://doi.org/10.1016/j.atmosres.2022.106045, 2022.

Guo, J., Li, Y., Cohen, J. B., Li, J., Chen, D., Xu, H., Liu, L., Yin, J., Hu, K., and Zhai, P.: Shift in the temporal trend of boundary layer height in China using long-term (1979–2016) radiosonde data, Geophys. Res. Lett., 46, 6080–6089, https://doi.org/10.1029/2019GL082666, 2019.

Guo, J., Zhang, J., Yang, K., Liao, H., Zhang, S., Huang, K., Lv, Y., Shao, J., Yu, T., Tong, B., Li, J., Su, T., Yim, S. H. L., Stoffelen, A., Zhai, P., and Xu, X.: Investigation of near-global daytime boundary layer height using high-resolution radiosondes: first results and comparison with ERA5, MERRA-2, JRA-55, and NCEP-2 reanalyses, Atmospheric Chem. Phys., 21, 17079–17097, https://doi.org/10.5194/acp-21-17079-2021, 2021.

Hu, F., Xie, P., Xu, J., Li, A., Lv, Y., Zhang, Z., Zheng, J., and Tian, X.: Impacts of synoptic weather patterns on hefei's ozone in warm season and analysis of transport pathways during extreme pollution events, J. Environ. Sci., https://doi.org/10.1016/j.jes.2024.06.032, 2024.

Huang, M., Gao, Z., Miao, S., Chen, F., LeMone, M. A., Li, J., Hu, F., and Wang, L.: Estimate of boundary-layer depth over beijing, china, using doppler lidar data during SURF-2015, Bound.-Layer Meteorol., 162, 503–522, https://doi.org/10.1007/s10546-016-0205-2, 2017.

Jia, M., Yuan, J., Wang, C., Xia, H., Wu, Y., Zhao, L., Wei, T., Wu, J., Wang, L., Gu, S. Y., Liu, L., Lu, D., Chen, R., Xue, X., and Dou, X.: Long-lived high-frequency gravity waves in the atmospheric boundary layer: Observations and simulations, Atmospheric Chem. Phys., 19, 15431–15446, https://doi.org/10.5194/acp-19-15431-2019, 2019.

Jiang, P., Yuan, J., Wu, K., Wang, L., and Xia, H.: Turbulence detection in the atmospheric boundary layer using coherent doppler wind lidar and microwave radiometer, Remote Sens., 14, 2951, https://doi.org/10.3390/rs14122951, 2022.

Justus, C. G., Hargraves, W. R., Mikhail, A., and Graber, D.: Methods for estimating wind speed frequency distributions, J. Appl. Meteorol., 17, 350–353, https://doi.org/10.1175/1520-0450(1978)017<0350:MFEWSF>2.0.CO;2, 1978.

Kang, H., Zhu, B., Gao, J., He, Y., Wang, H., Su, J., Pan, C., Zhu, T., and Yu, B.: Potential impacts of cold frontal passage on air quality over the Yangtze River delta, china, Atmospheric Chem. Phys., 19, 3673–3685, https://doi.org/10.5194/acp-19-3673-

2019, 2019.

Kim, C. P. and Entekhabi, D.: Feedbacks in the land-surface and mixed-layer energy budgets, Bound.-Layer Meteorol., 88, 1–21, https://doi.org/10.1023/A:1001094008513, 1998.

Kotthaus, S., Bravo-Aranda, J. A., Collaud Coen, M., Guerrero-Rascado, J. L., Costa, M. J., Cimini, D., O'Connor, E. J., Hervo, M., Alados-Arboledas, L., Jiménez-Portaz, M., Mona, L., Ruffieux, D., Illingworth, A., and Haeffelin, M.: Atmospheric boundary layer height from ground-based remote sensing: a review of capabilities and limitations, Atmospheric Meas. Tech., 16, 433–479, https://doi.org/10.5194/amt-16-433-2023, 2023.

Li, C., Li, H., Zhang, Y., Zha, D., Zhao, B., Yang, S., Zhang, B., and De Boer, W. F.: Predicting hydrological impacts of the Yangtze-to-huaihe water diversion project on habitat availability for wintering waterbirds at caizi lake, J. Environ. Manage., 249, 109251, https://doi.org/10.1016/j.jenvman.2019.07.022, 2019.

Li, L., Zhu, A., Huang, L., Wang, Q., Chen, Y., Ooi, M. C. G., Wang, M., Wang, Y., and Chan, A.: Modeling the impacts of land use/land cover change on meteorology and air quality during 2000–2018 in the Yangtze River delta region, china, Sci. Total Environ., 829, 154669, https://doi.org/10.1016/j.scitotenv.2022.154669, 2022a.

Li, L., Wang, Y., Lu, J., Wang, X., Wu, P., and Tao, Y.: Spatial and temporal variability of maximum wind speed and extreme wind speed in anhui province during different recurrence intervals from 1981 to 2020, J. Trop. Meteorol., 38, 662–670, https://doi.org/10.16032/j.issn.1004-4965.2022.060, 2022b.

Li, X., Li, Q.-P., Ding, Y.-H., and Wang, M.: Near-surface wind speed changes in eastern China during 1970–2019 winter and its possible causes, Adv. Clim. Change Res., 13, 228–239, https://doi.org/10.1016/j.accre.2022.01.003, 2022c.

Li, X.-B., Han, Y.-X., Fu, Z.-Y., Zhang, Y.-C., Fan, M., Sang, S.-J., Chen, X.-X., Liang, B.-Y., Liu, Y.-C., Lu, P.-C., Li, H.-W., Pan, H.-F., and Yang, J.-M.: Association of sudden sensorineural hearing loss with meteorological factors: a time series study in hefei, china, and a literature review, Environ. Sci. Pollut. Res., 31, 42970–42990, https://doi.org/10.1007/s11356-024-33943-1, 2024.

Li, Z., Guo, J., Ding, A., Liao, H., Liu, J., Sun, Y., Wang, T., Xue, H., Zhang, H., and Zhu, B.: Aerosol and boundary-layer interactions and impact on air quality, Natl. Sci. Rev., 4, 810–833, https://doi.org/10.1093/nsr/nwx117, 2017.

Li, Z., Song, L., Ma, H., Xiao, J., Wang, K., and Chen, L.: Observed surface wind speed declining induced by urbanization in east China, Clim. Dyn., 50, 735–749, https://doi.org/10.1007/s00382-017-3637-6, 2018.

Liu, H., Huang, X., Fei, J., Zhang, C., and Cheng, X.: Spatiotemporal features and associated synoptic patterns of extremely persistent heavy rainfall over china, J. Geophys. Res. Atmospheres, 127, e2022JD036604, https://doi.org/10.1029/2022JD036604, 2022.

Liu, L., Liang, Y., He, C., Li, B., Chu, L., and Li, J.: Evaluating the contribution of climate change and urbanization to the reversal in maximum surface wind speed decline: case study in the Yangtze River economic belt, china, Urban Clim., 52, 101713, https://doi.org/10.1016/j.uclim.2023.101713, 2023.

Liu, X., Guo, Q., Guo, Z., Yin, Z.-Y., Dong, B., and Smith, R.: Where were the monsoon regions and arid zones in Asia prior to the Tibetan Plateau uplift?, Natl. Sci. Rev., 2, 403–416, https://doi.org/10.1093/nsr/nwv068, 2015.

Madala, S., Satyanarayana, A. N. V., and Rao, T. N.: Performance evaluation of PBL and cumulus parameterization schemes of WRF ARW model in simulating severe thunderstorm events over gadanki MST radar facility — case study, Atmospheric Res., 139, 1–17, https://doi.org/10.1016/j.atmosres.2013.12.017, 2014.

Manninen, A. J., Marke, T., Tuononen, M., and O'Connor, E. J.: Atmospheric boundary layer classification with doppler lidar, J. Geophys. Res. Atmospheres, 123, 8172–8189, https://doi.org/10.1029/2017JD028169, 2018.

Mei, L., Wang, X., Gong, Z., Liu, K., Hua, D., and Wang, X.: Retrieval of the planetary boundary layer height from lidar measurements by a deep-learning method based on the wavelet covariance transform, Opt. Express, 30, 16297, https://doi.org/10.1364/OE.454094, 2022.

Miao, Y., Guo, J., Liu, S., Wei, W., Zhang, G., Lin, Y., and Zhai, P.: The climatology of low-level jet in beijing and guangzhou, china, J. Geophys. Res. Atmospheres, 123, 2816–2830, https://doi.org/10.1002/2017JD027321, 2018.

Mirza, A. K., Dacre, H. F., and Lo, C. H. B.: A case study analysis of the impact of a new free tropospheric turbulence scheme on the dispersion of an atmospheric tracer, Q. J. R. Meteorol. Soc., 150, 1907–1925, https://doi.org/10.1002/qj.4681, 2024.

O'Connor, E. J., Illingworth, A. J., Brooks, I. M., Westbrook, C. D., Hogan, R. J., Davies, F., and Brooks, B. J.: A method for estimating the turbulent kinetic energy dissipation rate from a vertically pointing doppler lidar, and independent evaluation from balloon-borne in situ measurements, J. Atmospheric Ocean. Technol., 27, 1652–1664, https://doi.org/10.1175/2010jtecha1455.1, 2010.

Ortiz-Amezcua, P., Andújar-Maqueda, J., Manninen, A. J., Pentikäinen, P., O'Connor, E. J., Stachlewska, I. S., De Arruda Moreira, G., Benavent-Oltra, J. A., Casquero-Vera, J. A., Poczta, P., Wang, D., Harenda, K. M., Chojnicki, B. H., Szczepanik, D. M., Janicka, Ł., Schüttemeyer, D., Alados-Arboledas, L., and Guerrero-Rascado, J. L.: Dynamics of the atmospheric boundary layer over two middle-latitude rural sites with doppler lidar, Atmospheric Res., 280, 106434, https://doi.org/10.1016/j.atmosres.2022.106434, 2022.

Parsons, D. B.: An explanation for intense frontal updrafts and narrow cold-frontal rainbands, J. Atmospheric Sci., 49, 1810–1825, https://doi.org/10.1175/1520-0469(1992)049<1810:AEFIFU>2.0.CO;2, 1992.

Petrosyan, A., Galperin, B., Larsen, S. E., Lewis, S. R., Määttänen, A., Read, P. L., Renno, N., Rogberg, L. P. H. T., Savijärvi, H.,

https://doi.org/10.5194/amt-2024-178
Preprint. Discussion started: 28 October 2024

Atmospheric Measurement Techniques Discussions

Siili, T., Spiga, A., Toigo, A., and Vázquez, L.: The martian atmospheric boundary layer, Rev. Geophys., 49, 2010RG000351, https://doi.org/10.1029/2010RG000351, 2011.

Pobočíková, I., Sedliačková, Z., and Michalková, M.: Application of four probability distributions for wind speed modeling, Procedia Eng., 192, 713–718, https://doi.org/10.1016/j.proeng.2017.06.123, 2017.

Qin, R. X., Xiao, C., Zhu, Y., Li, J., Yang, J., Gu, S., Xia, J., Su, B., Liu, Q., and Woodward, A.: The interactive effects between high temperature and air pollution on mortality: a time-series analysis in hefei, china, Sci. Total Environ., 575, 1530–1537, https://doi.org/10.1016/j.scitotenv.2016.10.033, 2017.

Qiu, Z., Xian, J., Yang, Y., Lu, C., Yang, H., Hu, Y., Sun, J., and Zhang, C.: Characteristics of coastal low-level jets in the boundary layer of the pearl river estuary, J. Mar. Sci. Eng., 11, 1128, https://doi.org/10.3390/jmse11061128, 2023.

Rife, D. L., Pinto, J. O., Monaghan, A. J., Davis, C. A., and Hannan, J. R.: Global distribution and characteristics of diurnally varying low-level jets, J. Clim., 23, 5041–5064, https://doi.org/10.1175/2010jcli3514.1, 2010.

Shen, L., Cheng, Y., Bai, X., Dai, H., Wei, X., Sun, L., Yang, Y., Zhang, J., Feng, Y., Li, Y. J., Chen, D.-R., Liu, J., and Gui, H.: Vertical profile of aerosol number size distribution during a haze pollution episode in hefei, china, Sci. Total Environ., 814, 152693, https://doi.org/10.1016/j.scitotenv.2021.152693, 2022.

Shi, C., Roth, M., Zhang, H., and Li, Z.: Impacts of urbanization on long-term fog variation in anhui province, china, Atmos. Environ., 42, 8484–8492, https://doi.org/10.1016/j.atmosenv.2008.08.002, 2008.

Sisterson, D. L. and Frenzen, P.: Nocturnal boundary-layer wind maxima and the problem of wind power assessment., Environ. Sci. Technol., 12, 218–221, https://doi.org/10.1021/es60138a014, 1978.

Smalikho, I.: Techniques of wind vector estimation from data measured with a scanning coherent doppler lidar, J. Atmospheric Ocean. Technol., 20, 276–291, https://doi.org/10.1175/1520-0426(2003)020<0276:TOWVEF>2.0.CO;2, 2003.

Stull, R. B.: An introduction to boundary layer meteorology, Springer Science & Business Media, 688 pp., 1988.

Su, L., Lu, C., Yuan, J., Wang, X., He, Q., and Xia, H.: Measurement report: the promotion of low-level jet and thermal-effect on development of deep convective boundary layer at the southern edge of the taklimakan desert, https://doi.org/10.5194/egusphere-2024-1010, 15 May 2024.

Su, T., Li, Z., and Kahn, R.: Relationships between the planetary boundary layer height and surface pollutants derived from lidar observations over china: regional pattern and influencing factors, Atmospheric Chem. Phys., 18, 15921–15935, https://doi.org/10.5194/acp-18-15921-2018, 2018.

Su, T., Li, Z., and Kahn, R.: A new method to retrieve the diurnal variability of planetary boundary layer height from lidar under different thermodynamic stability conditions, Remote Sens. Environ., 237, 111519, https://doi.org/10.1016/j.rse.2019.111519, 2020.

Sun, J. and Ongsomwang, S.: Impact of multitemporal land use and land cover change on land surface temperature due to urbanization in hefei city, china, ISPRS Int. J. Geo-Inf., 10, 809, https://doi.org/10.3390/ijgi10120809, 2021.

Sun, Y., Yin, H., Liu, C., Mahieu, E., Notholt, J., Té, Y., Lu, X., Palm, M., Wang, W., Shan, C., Hu, Q., Qin, M., Tian, Y., and Zheng, B.: The reduction in C2H6 from 2015 to 2020 over hefei, eastern China, points to air quality improvement in China, Atmospheric Chem. Phys., 21, 11759–11779, https://doi.org/10.5194/acp-21-11759-2021, 2021.

Tamarin-Brodsky, T. and Hadas, O.: The asymmetry of vertical velocity in current and future climate, Geophys. Res. Lett., 46, 374–382, https://doi.org/10.1029/2018GL080363, 2019.

Tuononen, M., O'Connor, E. J., Sinclair, V. A., and Vakkari, V.: Low-level jets over utö, finland, based on doppler lidar observations, J. Appl. Meteorol. Climatol., 56, 2577–2594, https://doi.org/10.1175/JAMC-D-16-0411.1, 2017.

Vivone, G., D'Amico, G., Summa, D., Lolli, S., Amodeo, A., Bortoli, D., and Pappalardo, G.: Atmospheric boundary layer height estimation from aerosol lidar: a new approach based on morphological image processing techniques, Atmospheric Chem. Phys., 21, 4249–4265, https://doi.org/10.5194/acp-21-4249-2021, 2021.

Wang, C., Zhou, J., Zhou, S., Zhang, Y., and Zhang, M.: Distribution characteristics of wind in anhui province during 1981 -2012, J. Arid Meteorol., 33, 236–243, https://doi.org/10.11755/i.issn.1006-7639(2015)-02-0236, 2015a.

Wang, C., Jia, M., Xia, H., Wu, Y., Wei, T., Shang, X., Yang, C., Xue, X., and Dou, X.: Relationship analysis of PM2.5 and boundary layer height using an aerosol and turbulence detection lidar, Atmospheric Meas. Tech., 12, 3303–3315, https://doi.org/10.5194/amt-12-3303-2019, 2019.

Wang, H., Li, Z., Lv, Y., Zhang, Y., Xu, H., Guo, J., and Goloub, P.: Determination and climatology of the diurnal cycle of the atmospheric mixing layer height over beijing 2013–2018: lidar measurements and implications for air pollution, Atmospheric Chem. Phys., 20, 8839–8854, https://doi.org/10.5194/acp-20-8839-2020, 2020.

Wang, L., Qiang, W., Xia, H., Wei, T., Yuan, J., and Jiang, P.: Robust solution for boundary layer height detections with coherent doppler wind lidar, Adv. Atmospheric Sci., 38, 1920–1928, https://doi.org/10.1007/s00376-021-1068-0, 2021.

Wang, M., Fang, X., Hu, S., Hu, H., Li, T., and Dou, X.: Variation characteristics of water vapor distribution during 2000-2008 over hefei (31.9°N, 117.2°E) observed by L625 lidar, Atmospheric Res., 164–165, 1–8, https://doi.org/10.1016/j.atmosres.2015.04.003, 2015b.

Wang, M., Wei, T., Lolli, S., Wu, K., Wang, Y., Hu, H., Yuan, J., Tang, D., and Xia, H.: A long-term doppler wind LiDAR study of heavy pollution episodes in western Yangtze River delta region, china, Atmospheric Res., 310, 107616, https://doi.org/10.1016/j.atmosres.2024.107616, 2024.

Wang, S., Wang, Q., Jordan, R. E., and Persson, P. O. G.: Interactions among longwave radiation of clouds, turbulence, and snow surface temperature in the arctic: a model sensitivity study, J. Geophys. Res. Atmospheres, 106, 15323–15333, https://doi.org/10.1029/2000JD900358, 2001.

Wei, T., Xia, H., Hu, J., Wang, C., Shangguan, M., Wang, L., Jia, M., and Dou, X.: Simultaneous wind and rainfall detection by power spectrum analysis using a VAD scanning coherent doppler lidar, Opt. Express, 27, 31235, https://doi.org/10.1364/OE.27.031235, 2019.

Wei, T., Xia, H., Wu, Y., Yuan, J., Wang, C., and Dou, X.: Inversion probability enhancement of all-fiber CDWL by noise modeling and robust fitting, Opt. Express, 28, 29662, https://doi.org/10.1364/oe.401054, 2020.

Wei, T., Xia, H., Yue, B., Wu, Y., and Liu, Q.: Remote sensing of raindrop size distribution using the coherent doppler lidar, Opt. Express, 29, 17246, https://doi.org/10.1364/OE.426326, 2021.

Wei, T., Xia, H., Wu, K., Yang, Y., Liu, Q., and Ding, W.: Dark/bright band of a melting layer detected by coherent doppler lidar and micro rain radar, Opt. Express, 30, 3654, https://doi.org/10.1364/OE.450714, 2022.

Wei, W., Wu, B. G., Ye, X. X., Wang, H. X., and Zhang, H. S.: Characteristics and mechanisms of low-level jets in the Yangtze River delta of China, Bound.-Layer Meteorol., 149, 403–424, https://doi.org/10.1007/s10546-013-9852-8, 2013.

Wood, R., Wyant, M., Bretherton, C. S., Rémillard, J., Kollias, P., Fletcher, J., Stemmler, J., De Szoeke, S., Yuter, S., Miller, M., Mechem, D., Tselioudis, G., Chiu, J. C., Mann, J. A. L., O'Connor, E. J., Hogan, R. J., Dong, X., Miller, M., Ghate, V., Jefferson, A., Min, Q., Minnis, P., Palikonda, R., Albrecht, B., Luke, E., Hannay, C., and Lin, Y.: Clouds, aerosols, and precipitation in the marine boundary layer: an arm mobile facility deployment, Bull. Am. Meteorol. Soc., 96, 419–440, https://doi.org/10.1175/BAMS-D-13-00180.1, 2015.

Wyngaard, J. C.: Structure of the PBL, in: Lectures on Air Pollution Modeling, edited by: Venkatram, A. and Wyngaard, J. C., American Meteorological Society, Boston, MA, 9–61, https://doi.org/10.1007/978-1-935704-16-4_2, 1988.

Xia, H., Shentu, G., Shangguan, M., Xia, X., Jia, X., Wang, C., Zhang, J., Pelc, J. S., Fejer, M. M., Zhang, Q., Dou, X., and Pan, J.: Long-range micro-pulse aerosol lidar at 1.5 μm with an upconversion single-photon detector, Opt. Lett., 40, 1579, https://doi.org/10.1364/OL.40.001579, 2015.

Xia, H., Shangguan, M., Wang, C., Shentu, G., Qiu, J., Zhang, Q., Dou, X., and Pan, J.: Micro-pulse upconversion doppler lidar for wind and visibility detection in the atmospheric boundary layer, Opt. Lett., 41, 5218, https://doi.org/10.1364/ol.41.005218, 2016.

Xia H., Chen Y., Yuan J., Su L., Yuan Z., Huang S., and Zhao D.: Windshear detection in rain using a 30 km radius coherent doppler wind lidar at mega airport in plateau, Remote Sens., 16, 924, https://doi.org/10.3390/rs16050924, 2024.

Xue, L., Zhou, D., Huang, X., Lou, S., and Ding, A.: Climatological characteristics of cold fronts and their impacts on air quality in cold seasons over the eastern China, J. Geophys. Res. Atmospheres, 127, e2022JD037488, https://doi.org/10.1029/2022JD037488, 2022.

Yan, Y., Cai, X., Wang, X., Miao, Y., and Song, Y.: Low-level jet climatology of China derived from long-term radiosonde observations, J. Geophys. Res. Atmospheres, 126, e2021JD035323, https://doi.org/10.1029/2021JD035323, 2021.

Yan, Y., Cai, X., Miao, Y., and Yu, M.: Synoptic condition and boundary layer structure regulate PM2.5 pollution in the huaihe river basin, china, Atmospheric Res., 269, 106041, https://doi.org/10.1016/j.atmosres.2022.106041, 2022.

Yang, B., Finn, D., Rich, J., Gao, Z., and Liu, H.: Effects of low-level jets on near-surface turbulence and wind direction changes in the nocturnal boundary layer, J. Geophys. Res. Atmospheres, 128, e2022JD037657, https://doi.org/10.1029/2022JD037657, 2023.

Yang, Y., Fan, S., Wang, L., Gao, Z., Zhang, Y., Zou, H., Miao, S., Li, Y., Huang, M., Yim, S. H. L., and Lolli, S.: Diurnal evolution of the wintertime boundary layer in urban beijing, china: insights from doppler lidar and a 325-m meteorological tower, Remote Sens., 12, 3935, https://doi.org/10.3390/rs12233935, 2020.

Yin, J., Gao, C. Y., Hong, J., Gao, Z., Li, Y., Li, X., Fan, S., and Zhu, B.: Surface meteorological conditions and boundary layer height variations during an air pollution episode in nanjing, china, J. Geophys. Res. Atmospheres, 124, 3350–3364, https://doi.org/10.1029/2018JD029848, 2019.

Yuan, J., Xia, H., Wei, T., Wang, L., Yue, B., and Wu, Y.: Identifying cloud, precipitation, windshear, and turbulence by deep analysis of the power spectrum of coherent doppler wind lidar, Opt. Express, 28, 37406, https://doi.org/10.1364/OE.412809, 2020.

Yue, M., Wang, M., Guo, J., Zhang, H., Dong, X., and Liu, Y.: Long-term trend comparison of planetary boundary layer height in observations and CMIP6 models over china, J. Clim., 34, 8237–8256, https://doi.org/10.1175/JCLI-D-20-1000.1, 2021.

Zhang, C., Ding, R., Xiao, C., Xu, Y., Cheng, H., Zhu, F., Lei, R., Di, D., Zhao, Q., and Cao, J.: Association between air pollution and cardiovascular mortality in hefei, china: a time-series analysis, Environ. Pollut., 229, 790–797, https://doi.org/10.1016/j.envpol.2017.06.022, 2017.

Zhang, F., Zhang, Q., Du, Y., and Kong, H.: Characteristics of coastal low-level jets in the bohai sea, china, during the early warm season, J. Geophys. Res. Atmospheres, 123, 13,763-13,774, https://doi.org/10.1029/2018JD029242, 2018.

Zhang, H., Zhang, X., Li, Q., Cai, X., Fan, S., Song, Y., Hu, F., Che, H., Quan, J., Kang, L., and Zhu, T.: Research progress on estimation of the atmospheric boundary layer height, J. Meteorol. Res., 34, 482–498, https://doi.org/10.1007/s13351-020-9910-3, 2020.

https://doi.org/10.5194/amt-2024-178
Preprint. Discussion started: 28 October 2024

Atmospheric Measurement Techniques
Discussions

Zhang, L., Zhang, H., Li, Q., Wei, W., Cai, X., Song, Y., Mamtimin, A., Wang, M., Yang, F., Wang, Y., and Zhou, C.: Turbulent mechanisms for the deep convective boundary layer in the taklimakan desert, Geophys. Res. Lett., 49, e2022GL099447, https://doi.org/10.1029/2022GL099447, 2022.

Zhang, Y., Zuo, Q., Wu, Q., Han, C., and Tao, J.: An integrated diagnostic framework for water resource spatial equilibrium considering water-economy-ecology nexus, J. Clean. Prod., 414, 137592, https://doi.org/10.1016/j.jclepro.2023.137592, 2023.

Zhao, P., Zhang, R., Liu, J., Zhou, X., and He, J.: Onset of southwesterly wind over eastern China and associated atmospheric circulation and rainfall, Clim. Dyn., 28, 797–811, https://doi.org/10.1007/s00382-006-0212-y, 2007.

Zhao, S., He, J., Dong, L., Qi, S., Yin, D., Chen, J., and Yu, Y.: Contrasting vertical circulation between severe and light air pollution inside a deep basin: results from the collaborative experiment of 3D boundary-layer meteorology and pollution at the sichuan basin (BLMP-SCB), Bull. Am. Meteorol. Soc., 104, E411–E434, https://doi.org/10.1175/BAMS-D-22-0150.1, 2023.

Zhao, W. and Zou, Y.: Hefei: an emerging city in inland china, Cities, 77, 158–169, https://doi.org/10.1016/j.cities.2018.01.008, 2018.

Zhou, J.: Lidar observations of asian dust over hefei, china, in spring 2000, J. Geophys. Res., 107, 4252, https://doi.org/10.1029/2001JD000802, 2002.

Zhu, F., Ding, R., Lei, R., Cheng, H., Liu, J., Shen, C., Zhang, C., Xu, Y., Xiao, C., Li, X., Zhang, J., and Cao, J.: The short-term effects of air pollution on respiratory diseases and lung cancer mortality in hefei: a time-series analysis, Respir. Med., 146, 57–65, https://doi.org/10.1016/j.rmed.2018.11.019, 2019.

Appendix A

Table A1. Key Operating Parameters of the Doppler Lidar System

Parameter	Parameter	Value
Laser	Wavelength (nm)	1548
	Pulse energy (μJ)	300
	Pulse duration (ns)	600
	Repetition rate (kHz)	10
	AOM frequency shift (MHz)	80
Telescope	Diameter (mm)	100
Data	Sampling frequency (MHz)	250
	Range gate length (m)	30/60/150
	Time resolution (s)	1
Scanning	Scanning mode	VAD
	Elevation angle (°)	60
	Azimuth angle (°)	0-300

https://doi.org/10.5194/amt-2024-178
Preprint. Discussion started: 28 October 2024

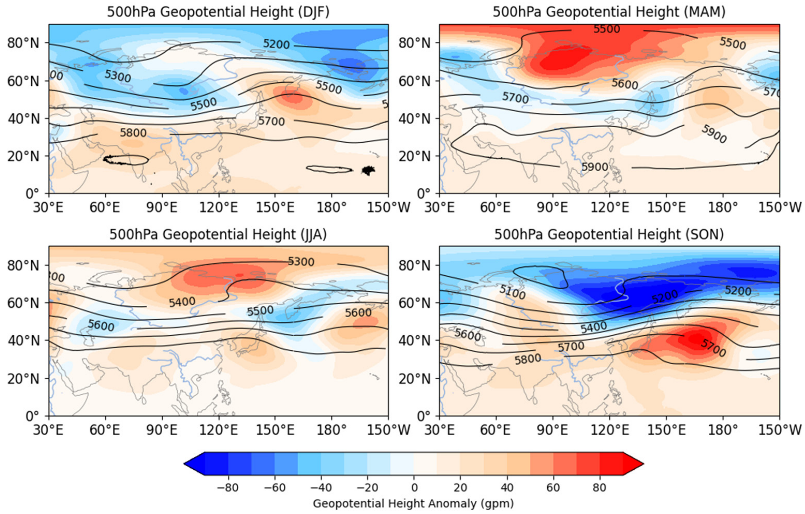

Figure A1. Seasonal distributions of 500-hPa geopotential height (contour, units: gpm) and geopotential height anomalies (shaded, units: gpm).